Uncertainty analysis for the integration of seismic and controlled source electro-magnetic data

Myoung Jae Kwon* and Roel Snieder

Center for Wave Phenomena, Department of Geophysics, Colorado School of Mines, 1500 Illinois St., Golden, CO 80401, USA

ABSTRACT

We study the appraisal problem for the joint inversion of seismic and controlled source electro-magnetic (CSEM) data and utilize rock-physics models to integrate these two disparate data sets. The appraisal problem is solved by adopting a Bayesian model and we incorporate four representative sources of uncertainty. These are uncertainties in 1) seismic wave velocity, 2) electric conductivity, 3) seismic data and 4) CSEM data. The uncertainties in porosity and water saturation are quantified by a posterior random sampling in the model space of porosity and water saturation in a marine one-dimensional structure. We study the relative contributions from the four individual sources of uncertainty by performing several statistical experiments. The uncertainties in the seismic wave velocity and electric conductivity play a more significant role on the variation of posterior uncertainty than do the seismic and CSEM data noise. The numerical simulations also show that the uncertainty in porosity is most affected by the uncertainty in the seismic wave velocity and that the uncertainty in water saturation is most influenced by the uncertainty in electric conductivity. The framework of the uncertainty analysis presented in this study can be utilized to effectively reduce the uncertainty of the porosity and water saturation derived from the integration of seismic and CSEM data.

Key words: Controlled source electro-magnetic, Metropolis-Hastings algorithm, Uncertainty analysis.

INTRODUCTION

The controlled source electro-magnetic (CSEM) method has been studied for the last few decades (Chave and Cox 1982; Cox *et al.* 1986) and its application for the delineation of a hydrocarbon reservoir has recently been discussed (Constable and Srnka 2007). Currently, there is an increasing interest in the integration of the seismic and CSEM methods in deep marine exploration (Harris and MacGregor 2006). Although the CSEM method has less resolution than the seismic method, it provides extra information about, for example, electric conductivity. This property is important for the economic evaluation of reservoirs. Therefore, the CSEM method is considered

an effective complementary tool when combined with seismic exploration.

The seismic and CSEM methods are disparate exploration techniques that are sensitive to different medium properties: the seismic method is sensitive to density and seismic wave velocity and the CSEM method to electric conductivity. There have been several approaches for joint inversion that integrate disparate data sets. Some of them assume a common structure (Musil, Maurer and Green 2003) or similar structural variations of different medium properties (Gallardo and Meju 2004; Hu, Abubakar and Habashy 2009). More recently, the application of rock-physics models for joint inversion has been studied (Hoversten *et al.* 2006). Rock-physics models enable us to interrelate seismic wave velocity and electric conductivity with the reservoir parameters such as porosity, water saturation, or permeability. The main advantage of the

*E-mail: mykwon@mines.edu

approach is that these reservoir parameters have great economic importance. The application of a rock-physics model is limited, however, by the fact that such a model is site-specific and there are not yet any universal solutions to the inverse problem. Furthermore, even for a particular area of interest, any rock-physics model is generally described as a cloud of samples. These limitations imply that joint inversion via a rock-physics model intrinsically necessitates a stochastic approach. Stochastic inversion has recently been studied for seismic inversion (Spikes *et al.* 2007) and joint inversion of seismic and CSEM data (Chen *et al.* 2007). The contributions of rock-physics model uncertainties are also being studied (Chen and Dickens 2009). Generally, the accuracy of joint inversion of seismic and CSEM data via rock-physics models is limited by the uncertainty of the rock-physics model as well as by data noise. The contribution of seismic and CSEM data noise on the joint inversion via rock-physics models, however, has not yet been studied. Moreover, it is not yet understood whether rock-physics model uncertainties play a more significant role than data noise on the joint inversion process.

We aim to investigate the relative contribution of different sources of overall uncertainty that arise when we use rock-physics models for joint inversion. These include seismic data noise, CSEM data noise and uncertainties of rock-physics models. We implement several numerical experiments that reflect scenarios we may encounter in practice and compare the uncertainties in the inferred parameters. The comparison reveals the relative contributions of different sources of uncertainty and we can utilize the procedure to more effectively reduce the uncertainty, depending on whether our interests focus on porosity or water saturation.

METHODOLOGY

The goal of geophysical inversion is to make quantitative inferences about the earth from noisy data. There are mainly two different approaches for attaining this goal: in one, the unknown models are assumed to be deterministic and one uses inversion methods such as Tikhonov regularization (Tikhonov and Arsenin 1977; Aster, Borchers and Thurber 2005); in the other, all the unknowns are random and one uses Bayesian methods (Bayes 1763; Ulrych, Sacchi and Woodbury 2001; Tarantola 2005). The object of this project is to provide a framework for Bayesian joint inversion that leads to model estimates and their uncertainties.

The connection between geophysical data $\mathbf{d}$ and model $\mathbf{m}$ is written as

$$\mathbf{d} = L[\mathbf{m}] + \mathbf{e} \tag{1}$$

where L denotes a linear or non-linear operator that maps the model into the data and $\mathbf{e}$ represents data measurement error. The details of the operator are presented in the modelling procedure section. Bayes' theorem relates conditional and marginal probabilities of data $\mathbf{d}$ and model $\mathbf{m}$ as follows (Tarantola 2005):

$$\pi(\mathbf{m}|\mathbf{d}) = \frac{\pi(\mathbf{m})\,f(\mathbf{d}|\mathbf{m})}{\pi(\mathbf{d})} \propto \pi(\mathbf{m})\,f(\mathbf{d}|\mathbf{m}), \tag{2}$$

where $\pi(\mathbf{m})$ is a prior probability in the sense that it does not take into account any information about data $\mathbf{d}$; $f(\mathbf{d}|\mathbf{m})$ is likelihood of data $\mathbf{d}$, given model $\mathbf{m}$; and $\pi(\mathbf{m}|\mathbf{d})$ is the posterior probability density that we are inferring.

Hierarchical Bayesian model

The *P*-wave velocity and electric conductivity are derived from two reservoir parameters: porosity and water saturation. These reservoir parameters are the target model parameters in this project. There are two layers of likelihood probabilities that have hierarchical dependency. The variables and their hierarchical dependencies are displayed in Fig. 1. The uppermost row represents prior probabilities of the reservoir parameters: the porosity ($\mathbf{m}_\phi$) and water saturation ($\mathbf{m}_{S_w}$). The middle row denotes the likelihoods of the *P*-wave velocity ($\mathbf{d}_{V_p}$) and logarithm of electric conductivity ($\mathbf{d}_{\sigma_e}$). Finally, the lowermost row represents the likelihoods of seismic ($\mathbf{d}_s$) and CSEM data ($\mathbf{d}_e$).

Within the Bayesian framework, the prior probabilities of the reservoir parameters are expressed as $\pi_{prior}(\mathbf{m}_\phi)$ and $\pi_{prior}(\mathbf{m}_{S_w})$. Likewise, four possible likelihoods are expressed as follows: the likelihoods of the *P*-wave velocity $f(\mathbf{d}_{V_p}|\mathbf{m}_\phi, \mathbf{m}_{S_w})$, logarithm of electric conductivity $f(\mathbf{d}_{\sigma_e}|\mathbf{m}_\phi, \mathbf{m}_{S_w})$, seismic data $f(\mathbf{d}_s|\mathbf{d}_{V_p})$ and CSEM data $f(\mathbf{d}_e|\mathbf{d}_{\sigma_e})$. Therefore, the posterior probabilities (π_{post}) of the porosity and water saturation are derived from the prior (π_{prior}) and likelihood (f) probabilities as follows:

$$\pi_{post}(\mathbf{m}_\phi, \mathbf{m}_{S_w}|\mathbf{d}_{V_p}, \mathbf{d}_{\sigma_e}, \mathbf{d}_s, \mathbf{d}_e)$$
$$\propto \pi_{prior}(\mathbf{m}_\phi)\pi_{prior}(\mathbf{m}_{S_w})\,f(\mathbf{d}_{V_p}|\mathbf{m}_\phi, \mathbf{m}_{S_w})$$
$$\times\, f(\mathbf{d}_{\sigma_e}|\mathbf{m}_\phi, \mathbf{m}_{S_w})\,f(\mathbf{d}_s|\mathbf{d}_{V_p})\,f(\mathbf{d}_e|\mathbf{d}_{\sigma_e}). \tag{3}$$

Equation (3) indicates that the posterior probability is proportional to the product of individual priors and likelihoods.

In statistics, the central limit theorem states that the sum of a sufficiently large number of identically distributed independent random variables follows a normal distribution. This implies that the normal distribution is a reasonable choice for describing probability. Therefore, throughout this project, we
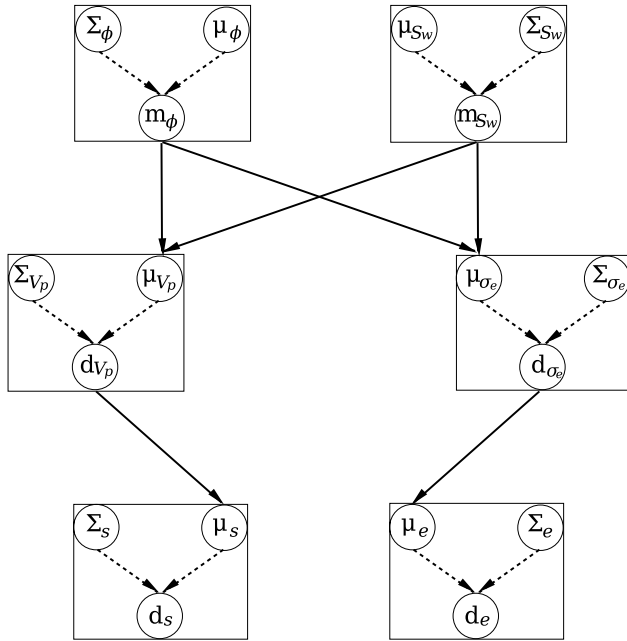
Figure 1 A hierarchical dependency structure represented by a directed graph. The nodes represent stochastic variables, the dashed arrows represent probability dependencies and the solid arrows represent deterministic relationships. μ and Σ denote expectation vectors and covariance matrices, respectively. $\mathbf{m}_\phi$ and $\mathbf{m}_{S_w}$ represent two reservoir parameters: medium porosity and water saturation. $\mathbf{d}_{V_p}$ and $\mathbf{d}_{\sigma_e}$ denote the P-wave velocity and logarithm of electric conductivity, respectively. $\mathbf{d}_s$ and $\mathbf{d}_e$ represent two different data sets: seismic and CSEM data.

assume that the priors and likelihoods generally follow multivariate Gaussian distribution with expectation vector μ and covariance matrix Σ, such that

$$f(\mathbf{x}) = \frac{1}{\sqrt{(2\pi)^n \det(\Sigma)}} \exp\left[-\frac{1}{2}(\mathbf{x}-\mu)^T \Sigma^{-1}(\mathbf{x}-\mu)\right], \qquad (4)$$

where $\mathbf{x}$ denotes data or model and n denotes the dimension of $\mathbf{x}$. Equation (4) expresses the general form of the probability function used in this project and the covariance matrices for individual prior and likelihoods are discussed later. Note that since the forward operations in this project (solid arrows in Fig. 1) are non-linear, the posterior distributions are not necessarily Gaussian.

Prior and likelihood model

In the Bayesian context, there are several approaches to represent prior information (Scales and Tenorio 2001). The prior model encompasses all the information we have before the data sets are acquired. In practice, the prior information in-

cludes the definition of the model parameters, geologic information about the investigation area and preliminary investigation results. Therefore, the prior model is the starting point of a Bayesian approach and we expect to have a posterior probability distribution with less uncertainty than the prior probability. The prior model plays an important role in Bayesian inversion by eliminating unreasonable models that also fit the data (Tenorio 2001). Obvious prior information we have is the definition of the porosity and water saturation, such that $0 \le m_{\phi_i} \le 1$ and $0 \le m_{S_{w_i}} \le 1$. This definition implies that the prior distributions of the porosity and water saturation are intrinsically non-Gaussian. Furthermore, there can be several fluid phases within the pore space, and the probability distribution of each fluid saturation can be described by a different distribution such as Dirichlet distribution (Gelman *et al.* 2003). In this study, we consider two fluid phases (gas and water) and assume that the variance of the water saturation is sufficiently small to warrant the assumption of Gaussian a priori probability density functions. We aim to assess the porosity and water saturation of the subsurface medium that has several layers. Generally, these reservoir parameters of each layer are correlated and have different variances. The assessment of the correlation and variance requires detailed analysis of geology and well logging data. In this study, we focus our study on the formulation of Bayesian joint inversion and, as a starting point, regard that the reservoir parameters of each layer are uncorrelated and have identical variance. In other words, we assume that the covariance matrices Σ_ϕ and Σ_{S_w} (Fig. 1) are diagonal and that the diagonal elements within each covariance matrix are identical.

For the hierarchical Bayesian model shown in Fig. 1, there are four elementary likelihoods. Each of these likelihoods describes how well any rock-physics model or geophysical forward modeling fits with the rock-physics experiment results or the noisy observations. The details of the likelihood modelling are covered in the modelling procedure section.

Markov-Chain Monte Carlo sampling

The assessment of the posterior probability requires great computational resources and, in most cases, is still impractical for 3D inverse problems. Pioneering studies about the assessment were performed for 1D seismic waveform inversion (Mosegaard *et al.* 1997; Gouveia and Scales 1998). The posterior model space of this project encompasses porosity and water saturation of several layers. We use a Markov-Chain Monte Carlo sampling method to indirectly estimate the posterior probability distribution of the porosity and water

saturation. In this project, the goal of the Markov-Chain Monte Carlo sampling method is to retrieve a set of samples, such that the sample distribution describes the joint posterior probability of equation (3). The Markov-Chain Monte Carlo sampling method is a useful tool to explore the space of feasible solutions and to investigate the resolution or uncertainty of the solution (Mosegaard and Sambridge 2002; Sambridge *et al.* 2006). The Metropolis-Hastings algorithm (Metropolis *et al.* 1953; Hastings 1970) and Gibbs sampler (Geman and Geman 1984) are the most widely used samplers for this purpose. We apply the Metropolis-Hastings algorithm for the assessment of posterior probability. The details of the Metropolis-Hastings algorithm are presented in Appendix A.

MODELLING PROCEDURES

The marine 1D model used in this research is shown in Fig. 2. The target layer, a gas saturated sandstone layer, is located between shale layers. The soft shale layer is modelled to have the highest clay content and the gas saturated sandstone layer to have the lowest clay content. The modelled values of the porosities ϕ, water saturations S_w, P-wave velocities V_p and electric conductivities σ_e are summarized in Table 1. The mean prior porosity μ_ϕ and water saturation μ_{S_w} values are assumed to be the modelled values.

Rock-physics likelihood modelling

Rock-physics models play a central role in the joint inversion presented here. However, in many cases the rock-physics models are site-specific and complicated functions of many
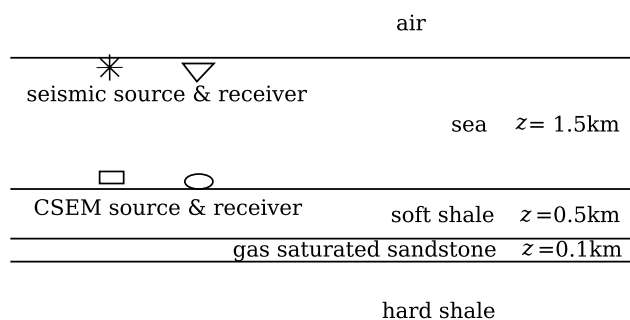
Table 1 The modelled values of porosity ϕ, water saturation S_w, P-wave velocities V_p, and electric conductivities σ_e of the 1D model shown in Fig. 2. ϕ_c is the critical porosity. K_d, K_0 and K_f denote the bulk modulus of the dry rock, mineral material and pore fluid, respectively. μ_0 is the shear modulus of the mineral material and ρ_w and ρ_0 are the density of the water phase and mineral material, respectively. σ_w denotes the electric conductivity of the water phase and m and n are the cementation and saturation exponents. CEC is the cation exchange capacity. A detailed explanation on the rock-physics parameters are presented in Appendix B.

	Soft shale	Gas saturated sandstone	Hard shale
ϕ (%)	35	25	10
S_w (%)	90	10	50
V_p (km/s)	2.28	3.56	4.88
σ_e (S/m)	0.580	0.007	0.044
ϕ_c (%)	60	40	40
K_w (MPa)	2.2	3.2	4.2
K_g (MPa)	0.03	0.03	0.03
K_0 (MPa)	16	36	40
μ_0 (MPa)	6	24	30
ρ_w (g/cc)	1	1	1
ρ_0 (g/cc)	2.55	2.65	2.75
σ_w (S/m)	3.33	3.33	3.33
m	2	2	2
n	2	2	2
CEC(C/kg)	10000	2000	6000

air

seismic source & receiver

sea z= 1.5km

CSEM source & receiver

soft shale z =0.5km

gas saturated sandstone z =0.1km

hard shale

Figure 2 The employed marine 1D model. Seismic source and receiver are located 10 m below the sea-surface. The CSEM source is located 1 m above the sea-bottom and the receiver is on the bottom. The earth is modelled as four homogeneous isotropic layers: seawater, soft shale, gas saturated sandstone and hard shale. The air and hard shale layer are two infinite half-spaces. The thicknesses (z) of the layers between the two half-spaces are fixed.

variables that include porosity, water saturation and clay content. Furthermore, there is an additional source of uncertainty associated with the choice of the rock-physics model. The motivation of this research is not to develop rock-physics models that better describe the earth and have smaller uncertainty. Instead, it is to understand the contribution of rock-physics model uncertainties on the overall uncertainty of joint inversion. However, by comparing the posterior density functions from different possible rock-physics models, we can deduce which rock-physics model better fits the given lithology. In this study, we utilize several empirical relations that are widely accepted. The quantitative dependence of the P-wave velocity and electric conductivity on porosity and water saturation is presented in Appendix B.

As stated in Appendix B, the distribution of the P-wave velocity is affected by several rock-physics parameters and, in the scale of geophysical exploration, there is no statistical model that universally describes the distribution of the P-wave velocity. The statistical description of P-wave velocity is therefore site-specific and involves detailed analysis of well logging data and laboratory experiments. The rough range

of the *P*-wave velocity of the earth minerals is 2–10 km/s (Mavko, Mukerji and Dvorkin 1998). In this study, we adopt the Gaussian distribution for the modelling of uncertainty of *P*-wave velocity. In contrast, considering that the electric conductivity exhibits exponential variation in most geologic environments (Palacky 1987), we assume that the electric conductivity follows a lognormal distribution. The *P*-wave velocity and electric conductivity are derived from empirical relations and Gaussian and log normal random numbers are thereafter added to the *P*-wave velocity and electric conductivity, respectively, to account for the uncertainty in the rock-physics model. Figures 3–6 show the simulated rock-physics models, where the porosity and water saturation samples of each layer is retrieved from the prior distributions. The distributions for the *P*-wave velocity indicate that the velocity is strongly dependent on the porosity and the contribution of the water saturation is less significant. In contrast, the distributions for the electric conductivity show that both the porosity and
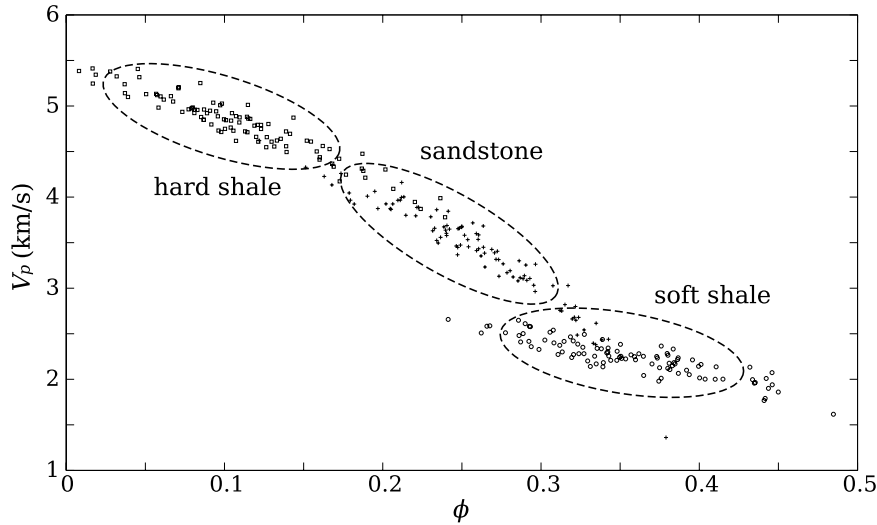
Figure 3 Simulated rock-physics model between porosity ϕ and *P*-wave velocity V_p. Among the three layers, the *P*-wave velocity depends least on the porosity in the soft shale layer. The quantitative dependence of the *P*-wave velocity on porosity is presented in Appendix B and Table 1.
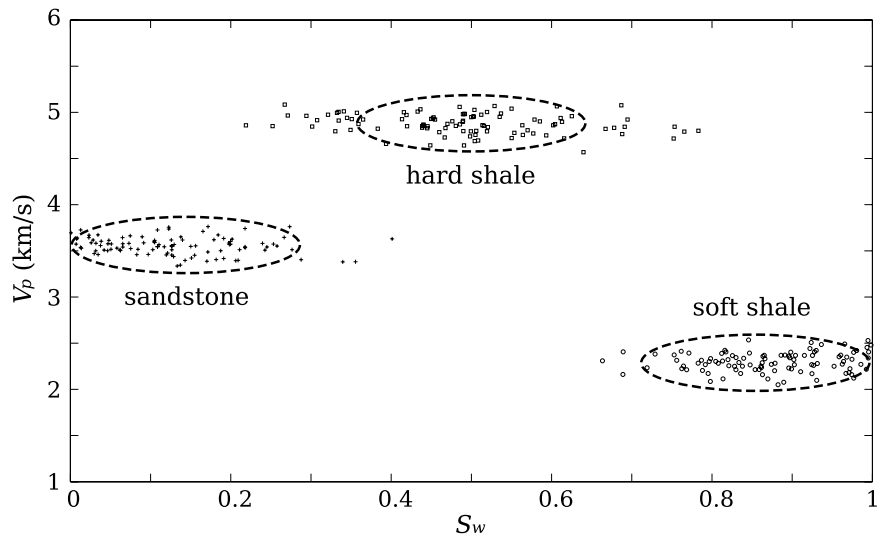

Figure 4 Simulated rock-physics model between water saturation S_w and *P*-wave velocity V_p. The *P*-wave velocity depends less on the water saturation than on the porosity. The quantitative dependence of the *P*-wave velocity on water saturation is presented in Appendix B and Table 1.
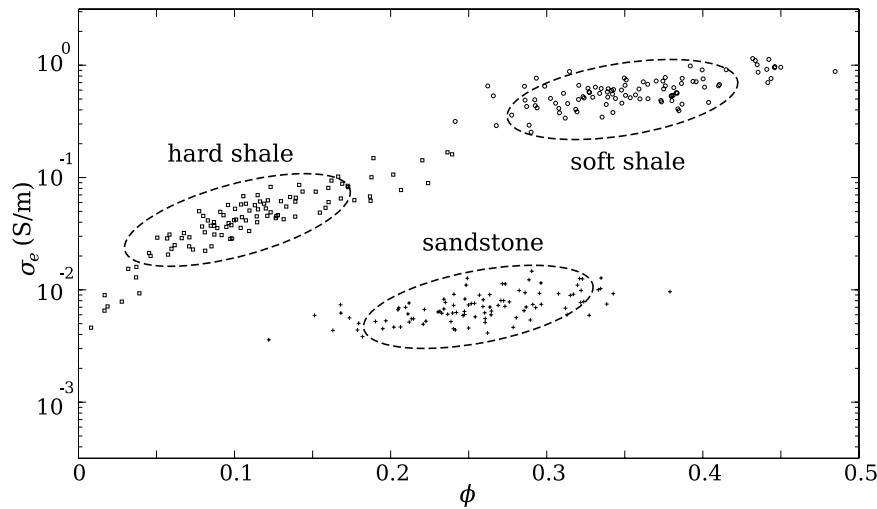
Figure 5 Simulated rock-physics model between porosity ϕ and electric conductivity σ_e. For each layer, increased porosity tends to accompany larger electric conductivity. The quantitative dependence of the electric conductivity on porosity is presented in Appendix B and Table 1.
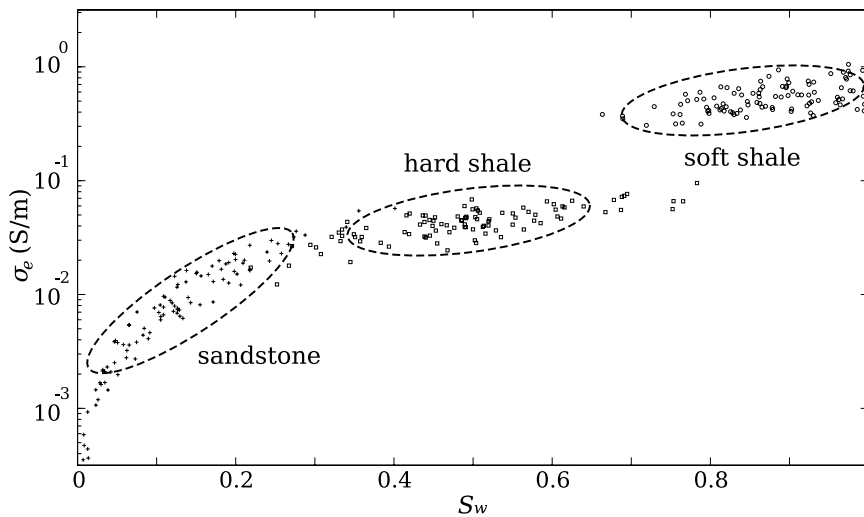

Figure 6 Simulated rock-physics model between water saturation S_w and electric conductivity σ_e. Among the three layers, the dependency of the electric conductivity on the water saturation is strongest in the sandstone layer. The quantitative dependence of the electric conductivity on water saturation is presented in Appendix B and Table 1.

water saturation influence the electric conductivity. Note that the dependencies are different for each layer. The dependency of the P-wave velocity on the porosity is weakest in the soft shale layer and the dependency of the electric conductivity on the water saturation is strongest in the sandstone layer. These differential dependencies in the different layers play a significant role in the joint inversion presented for this project.

We assume the likelihoods of the P-wave velocity $f(\mathbf{d}_{V_p}|\mathbf{m}_\phi, \mathbf{m}_{S_w})$ and logarithm of electric conductivity $f(\mathbf{d}_{\sigma_e}|\mathbf{m}_\phi, \mathbf{m}_{S_w})$ to follow the multivariate Gaussian distribu-

tion (equation (4)). Generally, the P-wave velocity and logarithm of electric conductivity of the layers are correlated and have different variance. The assessment of the correlation and variance requires a detailed analysis of geology and well logging data, which are beyond the scope of this study. For the evaluation of the likelihoods, we assume that the P-wave velocity and electric conductivity of each layer (Fig. 2) are independent. We model the covariance matrices $\boldsymbol{\Sigma}_{V_p}$ and $\boldsymbol{\Sigma}_{\sigma_e}$ (Fig. 1) as diagonal matrices whose diagonal elements are constants.

Seismic data likelihood modelling

There are many kinds of seismic data we can utilize: reflection data, traveltime data, amplitude versus offset or angle data and full waveform data. The full waveform data are the most general and encapsulate the largest amount of information. Seismic migration is the most common approach for handling full waveform data to reconstruct subsurface geometry. The application of the full waveform inversion is limited by its poor convergence speed. We use the waveform data for the joint inversion of seismic and CSEM data because the Monte Carlo method is effective for the least-squares misfit optimization for the velocities (Jannane *et al.* 1989; Snieder *et al.* 1989). Seismic waveform data are synthesized by a ray-tracing algorithm (Docherty 1987) and we model the primary reflections of the *P*-wave from the top and bottom boundaries of the target sandstone layer. There are many sources of seismic noise in a marine environment: ambient noise, guided waves, tail-buoy noise, shrimp noise, and side-scattered noise (Yilmaz 1987). We model the seismic noise by adding band-limited noise. The frequency band of the noise is between 10–55 Hz and the central frequency of the source wavelet is 30 Hz.

We assume that the seismic data likelihood probability $f(\mathbf{d}_s|\mathbf{d}_{V_p})$ follows the multivariate Gaussian distribution (equation (4)). For the calculation of the likelihood, it is necessary to evaluate the covariance matrix $\mathbf{\Sigma}_s$ (Fig. 1). For band-limited noise, the covariance matrix follows from the power spectrum of the bandpass filter and the resulting covariance matrix is not diagonal; a row of the covariance matrix is a sinc function. It is possible to derive the inverse covariance matrix from the above described covariance matrix. However, the inverse covariance matrix is generally unstable and we need to truncate the singular values of the covariance matrix, which yields an inverse matrix that has no significant improvement over the inverse of a diagonal matrix. We therefore approximate the covariance matrix of a band-limited noise as the covariance matrix of white noise. We model the covariance matrix $\mathbf{\Sigma}_s$ (Fig. 1) as a diagonal matrix whose diagonal elements are constant.

Controlled source electro-magnetic data likelihood modelling

The CSEM signal measured at a receiver location comprises three components. The first propagates through the solid earth and contains information on the reservoir properties. The second propagates through the seawater and attenuates rapidly. It is therefore only significant near the transmitter.

The third travels as a wave along the seawater-air interface (air-wave) and decreases with increasing water depth. In this project, the depth of the sea is 1.5 km and the air-wave is not significant.

Even though the deep sub-sea environment has little cultural noise, the CSEM measurements are not free from noise. These noise sources include the magneto-telluric signal, streaming potential and instrument noise. The magneto-telluric signal is significant at frequencies lower than 1 Hz. The streaming potential is generated by seawater movement. The natural background noise at frequencies around 1 Hz is about 1 pV/m (Chave and Cox 1982) and its influence can be minimized by using a stronger transmitter. The instrument noise is more important and mainly comes from the transmitter amplifier or receiver electrodes. At a lower frequency range, the noise from the amplifier and electrodes is proportional to $1/f$ and $1/\sqrt{f}$, respectively. On the other hand, the instrument noise is saturated at the higher frequency range, i.e., Johnson noise limit. Furthermore, the CSEM data quality is influenced by the positioning or aligning error of the transmitter and receiver locations/directions.

The CSEM data we utilize consists of the real and imaginary parts of the CSEM signal. We design the CSEM noise from the amplitude of the CSEM response and then add the noise to the real and imaginary parts of the response. The CSEM noise is categorized as systematic and non-systematic noise as shown in Fig. 7. The systematic noise includes instrument noise and positioning error. We assume the systematic noise to be proportional to the amplitude of the CSEM signal whereas the non-systematic noise is independent of the signal. A realization of noisy CSEM data is shown in Fig. 8, where the systematic noise is 5% of each noise-free amplitude and the non-systematic noise is 5×10^{-14} V/m. The CSEM signal decreases with frequency and the CSEM noise is more obvious.

We assume the CSEM data likelihood probability $f(\mathbf{d}_e|\mathbf{d}_{\sigma_e})$ follows the multivariate Gaussian distribution (equation (4)). For the calculation of the likelihood, we assume that the CSEM data noise is independent. We model the covariance matrix $\mathbf{\Sigma}_e$ (Fig. 1) as a diagonal matrix. Assuming that the systematic and non-systematic noise is uncorrelated, the diagonal element of the covariance matrix that corresponds to *i*-th datum (σ_i^2) is derived as

$$\sigma_i^2(d_e) = \sigma_i^2(\varepsilon_{\text{sys}}) + \sigma_i^2(\varepsilon_{\text{nonsys}}), \tag{5}$$

where ε_{sys} and $\varepsilon_{\text{nonsys}}$ denote the systematic and non-systematic noise, respectively. Note that $\sigma_i^2(\varepsilon_{\text{sys}})$ values decrease at
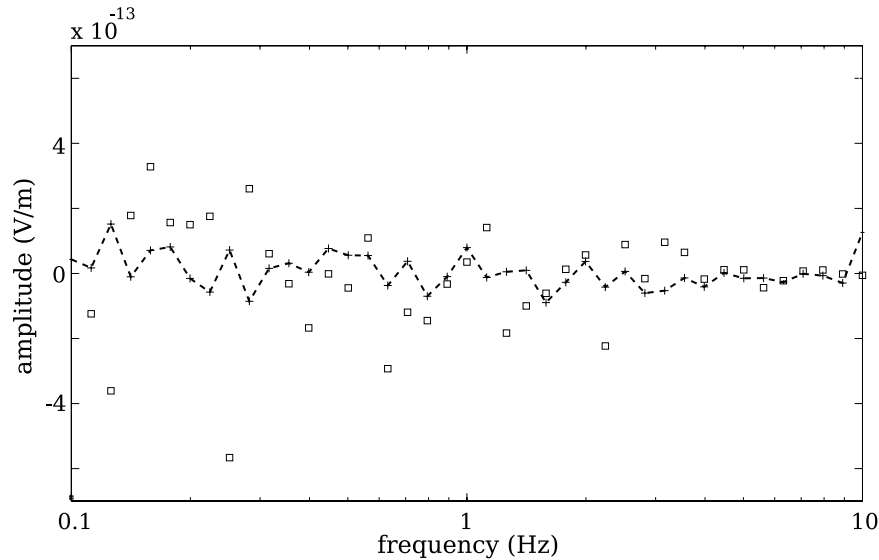
Figure 7 Two different types of CSEM noise: systematic noise (open dots) and non-systematic background noise (dashed curve). The systematic noise decreases with frequency. In contrast, the non-systematic noise is independent of frequency.
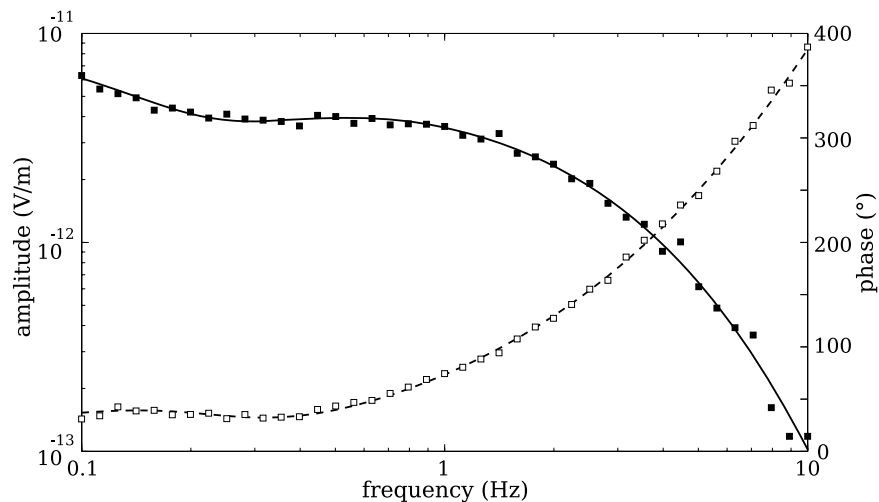

Figure 8 Electric field amplitude and phase response of a noise free (solid and dashed curves) and noise contaminated case (black and open dots). The exact electric conductivities used for the CSEM data calculation are shown here. The CSEM noise is significant in the high-frequency range.

the larger frequency whereas σ_i^2 (ε_{nonsys}) is independent of frequency.

UNCERTAINTY ANALYSIS

Histogram analysis of posterior distributions

We perform MCMC sampling to describe the posterior probability distribution (equation (3)). The random sampling is performed within a six-dimensional model space that accounts

for porosity or water saturation of soft shale, sandstone and hard shale layers (Fig. 2). The initial sample is drawn from the prior distribution and subsequent samplings are performed by the algorithm summarized in Appendix A. An example of the random sampling is shown in Fig. 9, which shows subsequent samples of the water saturation of the sandstone layer. In the given example, the initial sample is far away from the range of the posterior distribution and the initial movement of random samples toward posterior distribution, the burn-in stage, is clearly shown (shaded area). We exclude those samples from
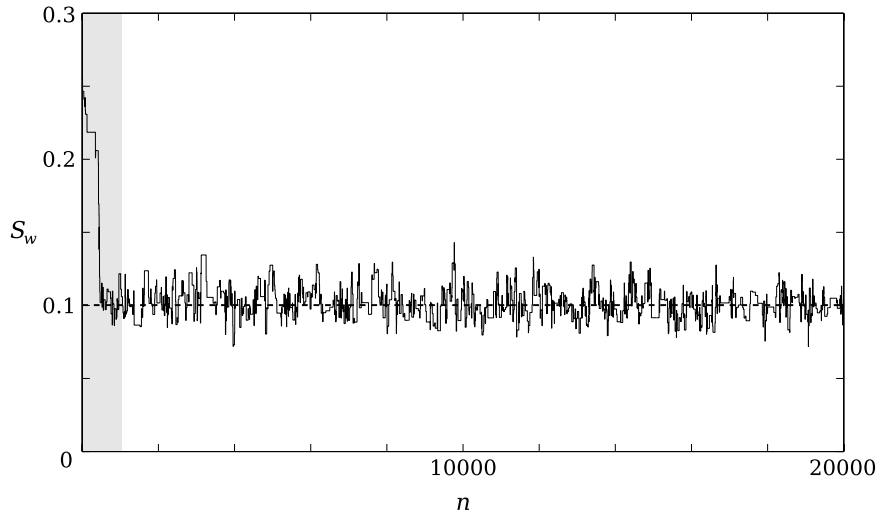
Figure 9 Samples of the water saturation (S_w) of the sandstone layer for subsequent samples with sampling number n. In the initial stage of random sampling (shaded area), the random sample is located away from the modelled value (dashed line) and shows gradual approach toward the posterior distribution (burn-in process). We discard the burn-in stage from the calculation of the sample variance.
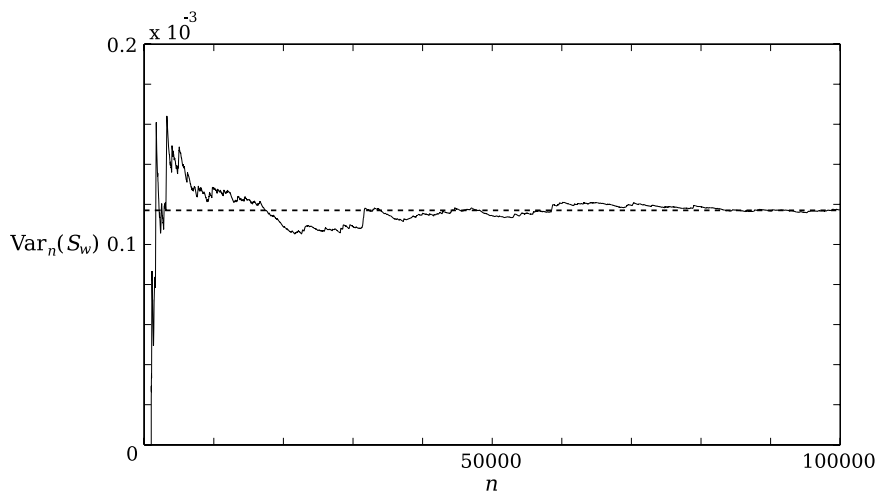

Figure 10 Convergence of the variance of the water saturation (S_w) as a function of the total number of samples. The burn-in samples are excluded from the calculation of the sample variance. For a sufficiently large sampling number n, the variance of the random samples converges to the posterior variance value (dashed line).

assessing the posterior distribution. For the diagnosis of the convergence of the random sampling toward the posterior distribution, we monitor the variance of the random samples as a function of the total number of samples (Fig. 10). For sufficiently large sampling number n, the variance of the random samples converges and we use this value for the variance of the posterior distribution.

The random samples of the porosity and water saturation are drawn from the posterior probability distribution of three different cases: using seismic data only, using CSEM data only and using both seismic and CSEM data. The uncertainty levels

applied to the comparison are summarized as the base state variances in Table 2. The posterior distributions of the porosity and water saturation of the target sandstone layer are summarized as histograms, as shown in Figs 11 and 12. Note that for the given uncertainties of the rock-physics model and data noise levels, the histograms show that the models based on seismic data or CSEM data alone weakly constrain porosity and water saturation. However, the histograms from the joint interpretation exhibit a narrower sample distribution of the porosity and water saturation. The figures also show that the seismic data are more sensitive to the porosity than to the wa-

Table 2 Two representative uncertainty levels used in the project.

Type of uncertainty source	Base state variance	Reduced state variance
Seismic wave velocity	$(0.1\,\text{km/s})^2$	$(0.03\,\text{km/s})^2$
Electric conductivity	$(0.1\log_{10}(\text{S/m}))^2$	$(0.03\log_{10}(\text{S/m}))^2$
Seismic noise	$(30\%\text{ of max. amplitude})^2$	$(10\%\text{ of max. amplitude})^2$
CSEM noise (systematic)	$(5\%\text{ of each amplitude})^2$	$(2\%\text{ of each amplitude})^2$
CSEM noise (non-systematic)	$(5\times10^{-14}\,\text{V/m})^2$	$(2\times10^{-14}\,\text{V/m})^2$
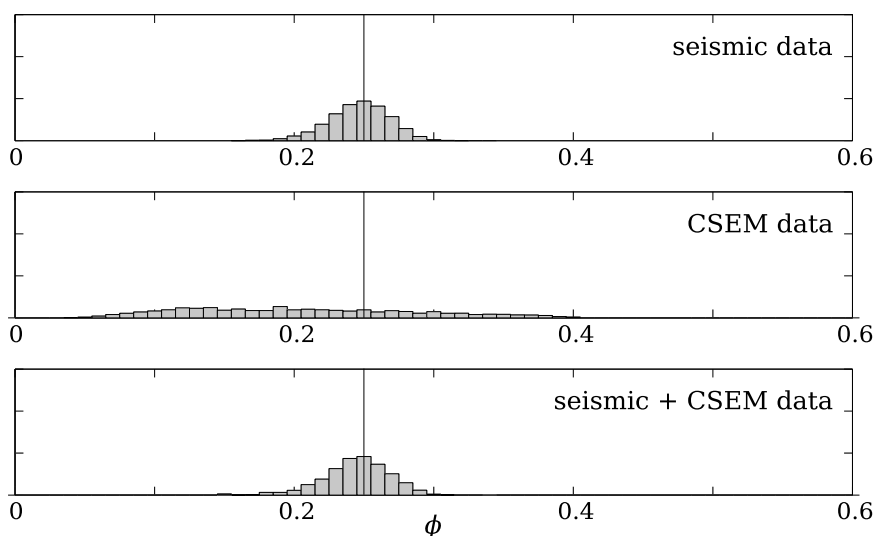
Figure 11 Histograms of posterior porosity (ϕ) samples of the sandstone layer. Vertical lines indicate the true porosity values.
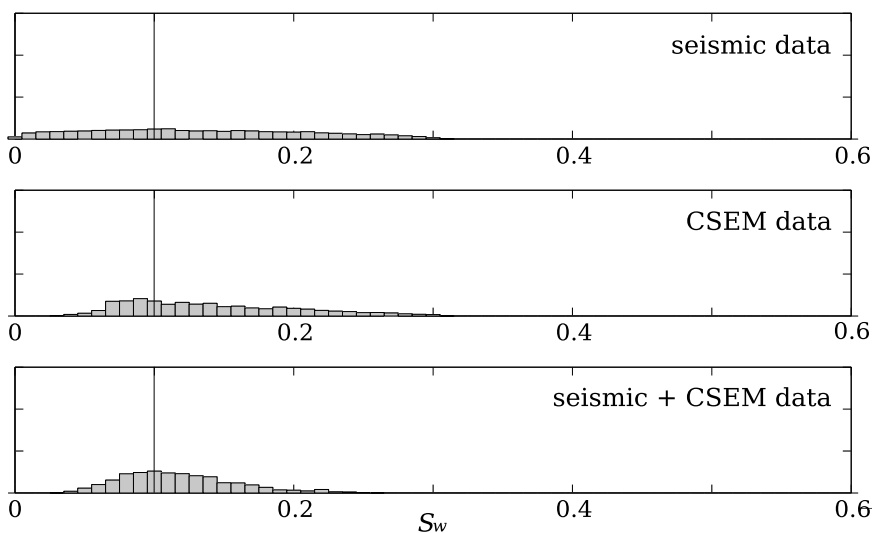
Figure 12 Histograms of posterior water saturation (S_w) samples of the sandstone layer. Vertical lines indicate the true water saturation values.

ter saturation. This is partly due to the rock-physics models in Figs 3 and 4, which show that the *P*-wave velocity has weaker correlation with the water saturation than with porosity. The relatively poor resolution from the CSEM data is attributed to the fact that the sandstone layer is electrically shielded by the more conductive overburden (soft shale layer). These examples illustrate the strength and limitation of both seismic and CSEM methods and explain the motivation of the joint

interpretation of seismic and CSEM data. The histograms of the joint interpretation show smaller posterior uncertainty than do the single interpretations. The reduction of uncertainty is more pronounced for water saturation than for porosity.

Next we compare the histograms that describe the posterior probabilities of different layers. Figure 13 shows the joint posterior distributions of the porosity of three layers. The posterior distribution for the soft shale layer is less constrained than

that of the other layers. This is a consequence of the relatively weak correlation between the porosity and *P*-wave velocity of the soft shale layer (Fig. 3). Despite the stronger sensitivity of the seismic and CSEM methods on the properties of the uppermost layer, the weaker correlations of the rock-physics model cause a larger variance of the porosity samples. The joint posterior distributions of the water saturation (Fig. 14) also exhibit that the posterior distribution for the soft shale layer is less constrained than for the sandstone layer and that
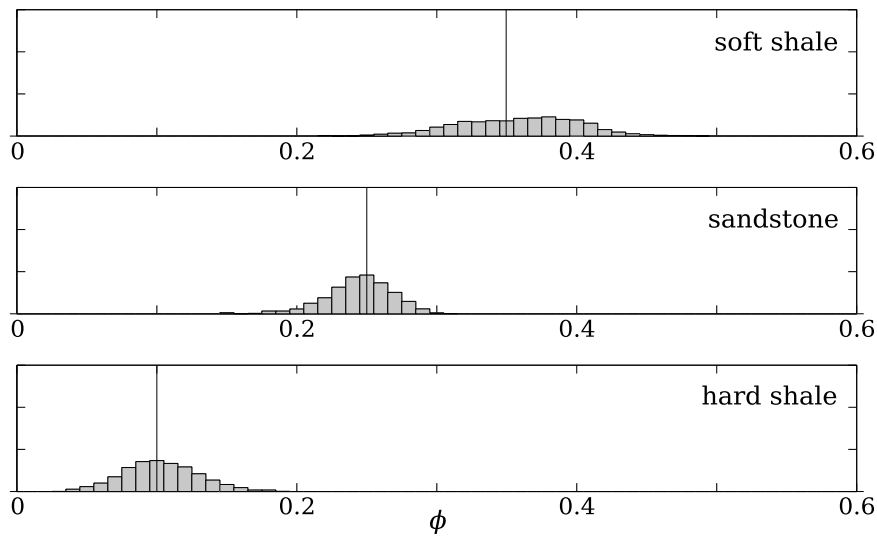

Figure 13 Histograms of posterior porosity (ϕ) samples of the three layers obtained from joint inversion of seismic and CSEM data (base uncertainty level). Vertical lines indicate the true porosity values.
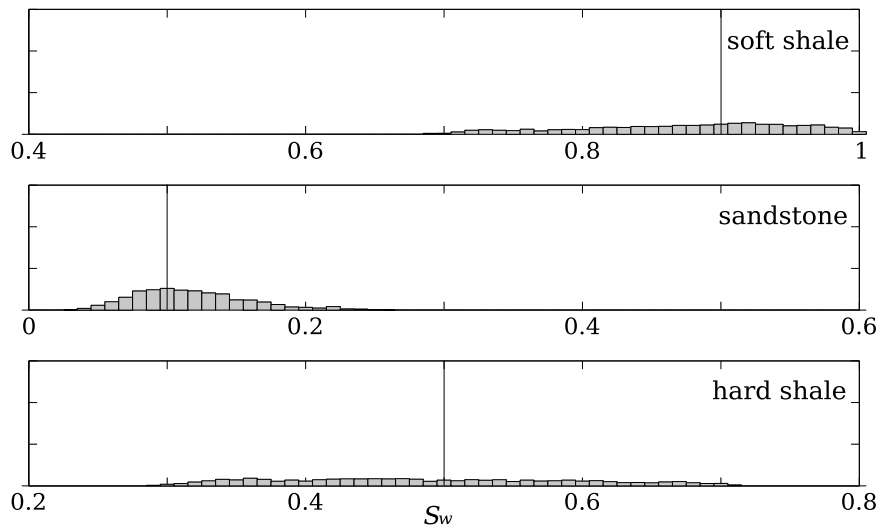

Figure 14 Histograms of posterior water saturation (S_w) samples of the three layers obtained from joint inversion of seismic and CSEM data (base uncertainty level). Vertical lines indicate the true water saturation values.

the rock-physics model uncertainty has more significance on constraining the posterior distribution than the resolution of the seismic and CSEM methods.

Finally, we study two representative uncertainty levels: a base state and a new state with reduced data uncertainties (Table 2). Note that the uncertainty of the electric conductivity is defined on a logarithmic scale. The seismic data uncertainty is defined as a ratio from the maximum amplitude value and the CSEM data uncertainty is defined as a sum of systematic and non-systematic noise. Figures 13 and 14 represent the posterior probability for the base uncertainty level.

The histograms for the reduced uncertainty level are shown in Figs 15 and 16. The reduced uncertainty level leads, of course, to a sharper posterior probability distribution than the base state and thus increases the accuracy in the estimates of porosity and water saturation. This stronger constraint is more obvious for porosity than for water saturation. This is due to the smaller resolution of the CSEM method compared to the seismic method.

The correlation of reservoir parameters between different layers can be studied by cross-plot analysis. An example of a cross-plot analysis is shown in Fig. 17, where the
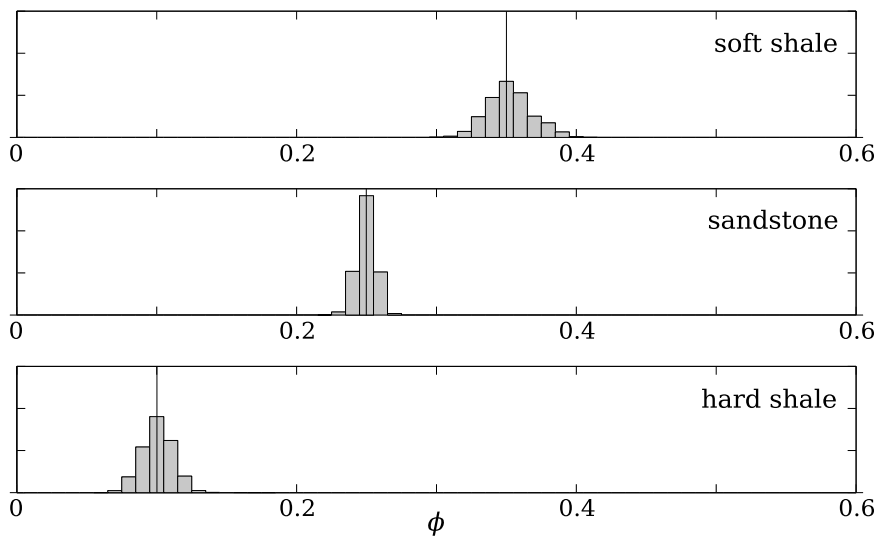

Figure 15 Histograms of posterior porosity (ϕ) samples of the three layers obtained from joint inversion of seismic and CSEM data (reduced uncertainty level). Vertical lines indicate the true porosity values.
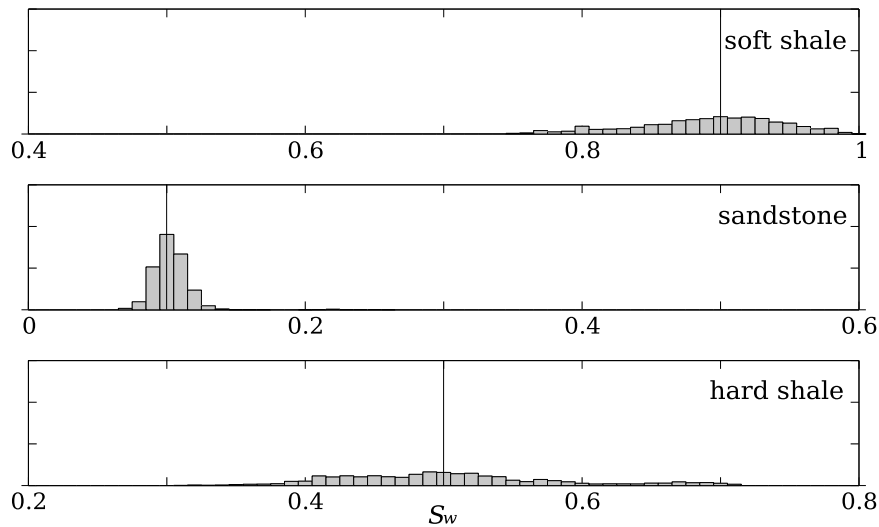

Figure 16 Histograms of posterior water saturation (S_w) samples of the three layers obtained from joint inversion of seismic and CSEM data (reduced uncertainty level). Vertical lines indicate the true water saturation values.
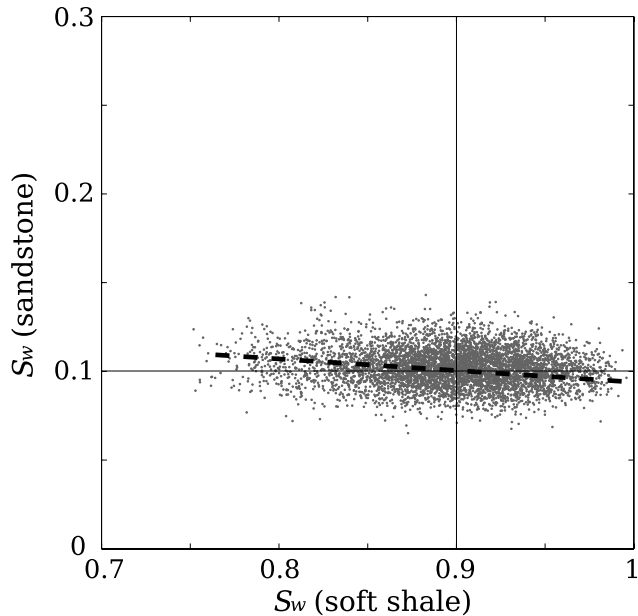
Figure 17 Cross-plot of posterior water saturation samples of the soft shale and sandstone layers. The histograms of the corresponding samples are shown in Fig. 16. The vertical and horizontal lines indicate the true water saturation values. The correlation coefficient between the two random variables is negative (dashed line).

posterior water saturation samples of the soft shale and sandstone layers are cross-plotted. The example demonstrates that the water saturation of the two layers has a negative correlation, which arises from the weak depth resolution of the CSEM exploration. Therefore, the correlation between the two layers becomes weaker as the thickness of the sandstone layer increases. The weaker correlation of a reservoir parameter between different layers generally accompanies reduced uncertainty of the reservoir parameter. The correlation analysis can help diagnose the trade-off between different model parameters.

Different scenarios for uncertainty reduction

In the previous section, we presented histograms that characterize the posterior uncertainty. As stated before, we assume the multivariate Gaussian distribution (equation (4)) for the calculation of prior and likelihood. There are however several factors that make the distribution of the posterior samples non-Gaussian. First, the porosity or water saturation has values between 0–1. Second, the porosity sampling is bounded by the critical porosity ϕ_c. The critical porosity is the threshold value between the suspension and the load-bearing domain

and denotes the upper porosity limit of the range where the rock-physics model can be applied (Mavko *et al.* 1998). The critical porosity values we apply for the soft shale, sandstone and hard shale layer are 0.6, 0.4, and 0.4, respectively. These bounds can lead to skewed sample distributions. Furthermore the posterior distributions do not necessarily follow the Gaussian distribution because of the non-linearity of the forward models. The posterior uncertainty can generally be assessed by sample mean and sample variance. For reasons of clarity, we use the Gaussian curves for the representation of the sample mean and sample variance.

In this project, we model four factors of uncertainty: rock-physics model uncertainties of the *P*-wave velocity and electric conductivity and noise of the seismic and CSEM data. We discussed the posterior probabilities of the porosity and water saturation for the base and reduced uncertainty levels (Table 2) in the previous section (Figs 13–16). We perform the following numerical experiments to quantify the contributions of the four possible sources of uncertainty. The initial simulation is performed based on the base uncertainty level. For analysis of the contributions of each of the factors on the posterior uncertainties, six subsequent simulations are performed with reduced uncertainty levels of one or two of the four factors of uncertainty. We perform the last simulation based on reduced uncertainty levels of all factors of uncertainty (reduced level). These eight numerical experiments are summarized in Table 3. We compare the posterior distributions from different treatments with the base and reduced levels and deduce how much a treatment contributes to the overall change of the sample variances. The posterior distributions of the porosity and water saturation are shown in Figs 18–23.

Table 3 Eight numerical experiments for the analysis of the contributions of four possible factors of uncertainty. Two states of uncertainty for the individual factors are listed in Table 2.

|	Uncertainty of the individual factors
Base level	None of the factors are reduced
Treatment-1	Only reducing *P*-wave velocity uncertainty
Treatment-2	Only reducing electric conductivity uncertainty
Treatment-3	Only reducing seismic noise level
Treatment-4	Only reducing CSEM noise level
Treatment-5	Reducing *P*-wave velocity uncertainty and seismic noise level
Treatment-6	Reducing electric conductivity uncertainty and CSEM noise level
Reduced level	Reducing all of the four uncertainty factors
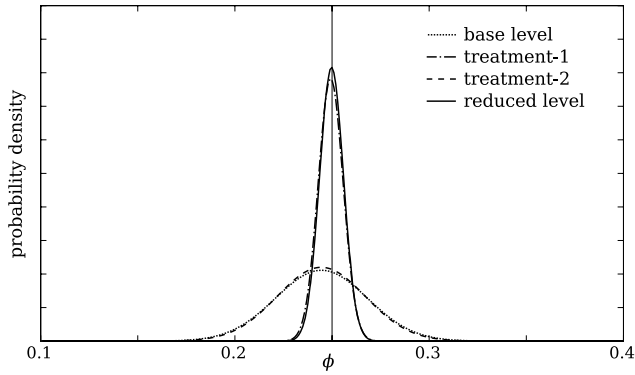
Figure 18 Posterior probability distributions of porosity ϕ of the sandstone layer. The distributions from treatments 1 and 2 (Table 3) are compared with those from the base and reduced levels. Vertical line indicates the true porosity value.
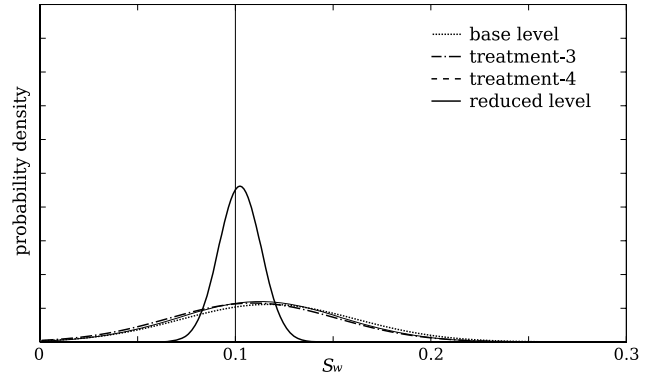

Figure 21 Posterior probability distributions of water saturation S_w of the sandstone layer. The distributions from treatments 3 and 4 (Table 3) are compared with those from the base and reduced levels. Vertical line indicates the true water saturation value.
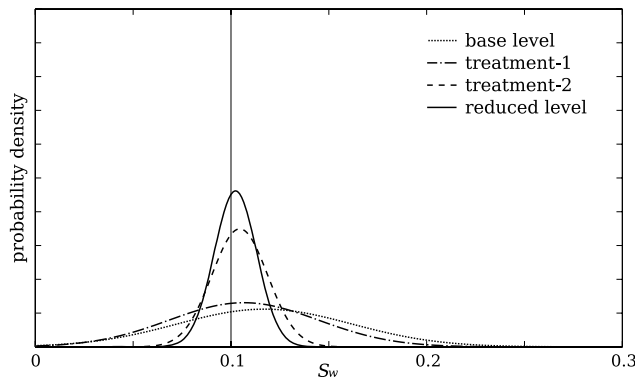

Figure 19 Posterior probability distributions of water saturation S_w of the sandstone layer. The distributions from treatments 1 and 2 (Table 3) are compared with those from the base and reduced levels. Vertical line indicates the true water saturation value.
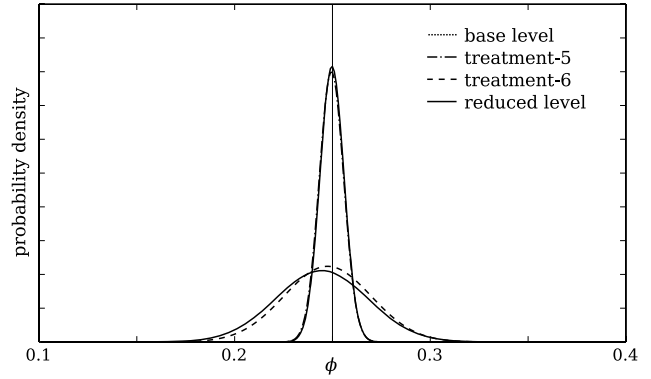

Figure 22 Posterior probability distributions of porosity ϕ of the sandstone layer. The distributions from treatments 5 and 6 (Table 3) are compared with those from the base and reduced levels. Vertical line indicates the true porosity value.

Figure 20 Posterior probability distributions of porosity ϕ of the sandstone layer. The distributions from treatments 3 and 4 (Table 3) are compared with those from the base and reduced levels. Vertical line indicates the true porosity value.
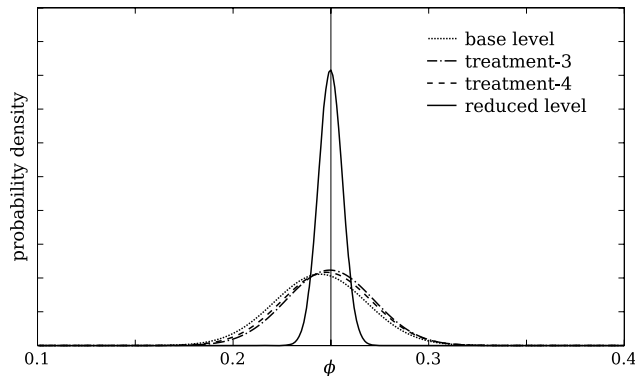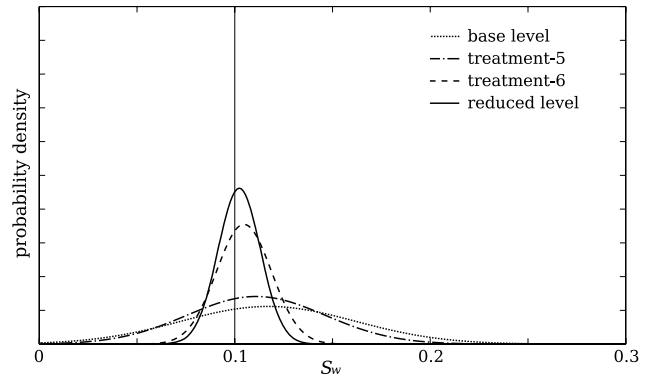

Figure 23 Posterior probability distributions of water saturation S_w of the sandstone layer. The distributions from treatments 5 and 6 (Table 3) are compared with those from the base and reduced levels. Vertical line indicates the true water saturation value.

Figures 18 and 19 show the posterior probability distributions acquired after performing the treatments 1 and 2. When we reduce uncertainty levels of the *P*-wave velocity or electric conductivity, the resultant posterior distributions exhibit smaller sample variances than the base level. Furthermore, the sample means are generally closer to the modelled values as we reduce the individual uncertainty levels. The probability density distribution for the porosity of the sandstone layer (Fig. 18) reveals that the *P*-wave velocity uncertainty plays a significant role on the overall uncertainty reduction of the porosity and the contribution of the electric conductivity uncertainty is limited. In contrast, Fig. 19 shows that the overall uncertainty variation of the water saturation is more strongly influenced by the uncertainty of the electric conductivity than by the uncertainty of the *P*-wave velocity. This is consistent with the simulated rock-physics models shown in Figs 3–6. From the rock-physics models, we can deduce that the porosity strongly influences both the *P*-wave velocity and electric conductivity. The rock-physics models also show that the water saturation strongly influences the electric conductivity while its influence on the *P*-wave velocity is limited.

The posterior probability distributions for treatments 3 and 4 are shown in Figs 20 and 21. When we reduce the noise levels of the seismic or CSEM data, the improvements of the posterior uncertainties of the porosity and water saturation are much less significant than the improvements due to the reduction of rock-physics model uncertainties. This shows that the overall uncertainty of the porosity and water saturation is more influenced by the rock-physics model uncertainties than by the noise of the seismic or CSEM data. The figures also show that for the given range of data noise, the seismic data noise reduction yields a more precise estimate than when the CSEM data noise is reduced.

Figures 22 and 23 show the posterior probability distributions for treatments 5 and 6. Compared to the single improvement cases, it is clear that the combined improvements give better assessments about the porosity and water saturation. The probability density distributions shown in Figs 22 and 23 are similar to the distributions shown in Figs 18 and 19. This implies that the posterior uncertainty variations from the combined improvements are mainly governed by the improvement of rock-physics model uncertainties and the contributions of the seismic and CSEM data noise are less significant.

The posterior probability distributions shown in Figs 18–23 are summarized in Table 4. The comparison of the variance values clearly show that the reductions of the sample variances of the porosity and water saturation are most strongly influenced by the uncertainty of the *P*-wave velocity and elec-

Table 4 Sample variances S^2 of porosity ϕ and water saturation S_w of the sandstone layer. The details about the treatments are in Table 3.

Sample variance ($\times 10^{-3}$)	$S^2 (\phi)$	$S^2 (S_w)$
Base level	0.560	1.997
Treatment-1	0.041	1.456
Treatment-2	0.516	0.205
Treatment-3	0.501	1.865
Treatment-4	0.532	1.728
Treatment-5	0.039	1.251
Treatment-6	0.498	0.198
Reduced level	0.038	0.117

tric conductivity, respectively. The contributions of the rock-physics model uncertainties on the posterior uncertainties are generally larger than those of the seismic and CSEM data noise. The numerical experiments suggest different ways of accomplishing uncertainty reduction depending on whether our interests focus on the porosity or water saturation. When porosity is our prime concern, we can effectively accomplish uncertainty reduction by improving the *P*-wave velocity model and by suppressing the seismic data noise. On the other hand, if we need a more accurate assessment of water saturation, the acquisition of more detailed electric conductivity information and the suppression of CSEM data noise are preferred.

Note that the above assessments are based on marginal analysis of posterior probability, and a possible correlation between different uncertainty factors is ignored. This can be misleading in the presence of strong correlation. The correlation between uncertainty factors can be analysed by the full factorial experiment (Fisher, Bennett and Yates 1990) that requires 2^n treatments, where n is the number of uncertainty factors.

CONCLUSIONS

We have shown that the posterior probability random sampling based on the Metropolis-Hastings algorithm is capable of assessing the multi-dimensional probability distribution of porosity and water saturation. We have also shown that the joint inversion of the seismic and CSEM data can be achieved by introducing rock-physics models that interconnect the *P*-wave velocity and electric conductivity. There are four representative sources of uncertainty that influence the posterior probability density of porosity and water saturation. These uncertainties are related to seismic wave velocity, electric

conductivity, seismic data and CSEM data. Even when single interpretations poorly constrain the posterior distributions of porosity and water saturation, the distributions from the joint interpretation are well constrained and exhibit reduced uncertainty.

Assuming two levels of overall uncertainty, we study the relative contributions from the four individual sources of uncertainty. The numerical simulations show that rock-physics model uncertainties play a more significant role on the overall uncertainty variation than do seismic and CSEM data noise. The numerical experiment also suggests different ways of accomplishing uncertainty reduction depending on whether our interests focus on porosity or on water saturation. When porosity is our prime concern, we can effectively accomplish uncertainty reduction by acquiring more precise *P*-wave velocity information and suppressing the seismic data noise. On the other hand, if we need a more accurate assessment of water saturation, the acquisition of more detailed electric conductivity information and the suppression of CSEM data noise are desirable.

We emphasize that the conclusions explained above depend on the parameters chosen in this project. Furthermore, there are many sources of uncertainty that we do not take into account such as lithological variations, variation of mineralogical composition of clay and depth of layers. If we include more of the data uncertainties, the balance between the uncertainties in the seismic wave velocity or electric conductivity and seismic or CSEM data noise can, therefore, be changed. The methodology of the uncertainty analysis presented in this project can, however, be extended to include those parameters and their uncertainties. The employed method can be used for experimental design and for targeting the source of the error that contributes most to the posterior uncertainty.

REFERENCES

Archie G.E. 1942. The electrical resistivity log as an aid in determining some reservoir characteristics. *Transactions of AIME* **146**, 54–62.

Aster R.C., Borchers B. and Thurber C.H. 2005. *Parameter Estimation and Inverse Problems*. Academic Press.

Batzle M. and Wang Z. 1992. Seismic properties of pore fluids. *Geophysics* **57**, 1396–1408.

Bayes R.T. 1763. An essay towards solving a problem in the doctrine of chances. *Philosophical Transactions of the Royal Society of London* **53**, 370–418.

Chave A. and Cox C.S. 1982. Controlled electromagnetic sources for measuring electrical conductivity beneath the oceans – 1. Forward problem and model study. *Journal of Geophysical Research* **87**, 5327–5338.

Chen J. and Dickens T.A. 2009. Effects of uncertainty in rock-physics models on reservoir parameter estimation using amplitude variation with angle and controlled-source electromagnetics data. *Geophysical Prospecting* **57**, 61–74.

Chen J., Hoversten G.M. Vasco D., Rubin Y. and Hou Z. 2007. A Bayesian model for gas saturation estimation using marine seismic AVA and CSEM data. *Geophysics* **72**, WA85–WA95.

Constable S. and Srnka L. 2007. An introduction to marine controlled-source electromagnetic methods for hydrocarbon exploration. *Geophysics* **72**, WA3–WA12.

Cox C.S., Constable S.C., Chave A.D. and Webb S.C. 1986. Controlled-source electromagnetic sounding of the oceanic lithosphere. *Nature* **320**, 52–54.

Docherty P. 1987. *Ray theoretical modeling, migration and inversion in two-and-one-half-dimensional layered acoustic media*. PhD thesis, Colorado School of Mines.

Fisher R.A., Bennett J.H. and Yates F. 1990. *Statistical Methods, Experimental Design, and Scientific Inference*. Oxford University Press.

Gallardo L.A. and Meju M.A. 2004. Joint two-dimensional DC resistivity and seismic travel time inversion with cross-gradients constraints. *Journal of Geophysical Research* **109**, B03311.

Gassmann F. 1951. Über die Elastizität poröser Medien. *Vierteljahrsschrift der Naturforschenden Gesellschaft in Zürich* **96**, 1–23.

Gelman A., Carlin J.B., Stern H.S. and Rubin D.B. 2003. *Bayesian Data Analysis*. Chapman and Hall.

Geman S. and Geman D. 1984. Stochastic relaxation, Gibbs distribution, and the Bayesian restoration of images. *IEEE Transactions on Pattern Analysis and Machine Intelligence* **6**, 721–741.

Gouveia W.P. and Scales J.A. 1998. Bayesian seismic waveform inversion: Parameter estimation and uncertainty analysis. *Journal of Geophysical Research* **103**, 2759–2779.

Han D. 1986. *Effects of porosity and clay content on acoustic properties of sandstones and unconsolidated sediments*. PhD thesis, Stanford University.

Han D. and Batzle M. 2004. Gassmann's equation and fluid-saturation effects on seismic velocities. *Geophysics* **69**, 398–405.

Harris P. and MacGregor L. 2006. Determination of reservoir properties from the integration of CSEM and seismic data. *First Break* **24**, 53–59.

Hastings W.K. 1970. Monte Carlo sampling methods using Markov Chains and their applications. *Biometrika* **57**, 97–109.

Hoversten G.M., Cassassuce F., Gasperikova E., Newman G.A., Chen J., Rubin Y. *et al.* 2006. Direct reservoir parameter estimation using joint inversion of marine seismic AVA and CSEM data. *Geophysics* **71**, C1–C13.

Hu W., Abubakar A. and Habashy T. 2009. Joint electromagnetic and seismic inverion using structural contraints. *Geophysics* **74**, R99–R109.

Jannane M., Beydoun W., Crase E., Cao D., Koren Z., Landa E. *et al.* 1989. Wavelengths of earth structures that can be resolved from seismic reflection data. *Geophysics* **54**, 906–910.

Kaipio J.P., Kolehmainen V., Somersalo E. and Vauhkonen M. 2000. Statistical inversion and Monte Carlo sampling methods in electrical impedance tomography. *Inverse Problems* **16**, 1487–1522.

Mavko G., Mukerji T. and Dvorkin J. 1998. *The Rock Physics Handbook*. Cambridge University Press.

Metropolis N., Rosenbluth A.W., Rosenbluth M.N. and Teller A.H. 1953. Equation of state calculations by fast computing machines. *The Journal of Chemical Physics* **21**, 1087–1092.

Mosegaard K. and Sambridge M. 2002. Monte Carlo analysis of inverse problems. *Inverse Problems* **18**, R29–R54.

Mosegaard K., Singh S., Snyder D. and Wagner H. 1997. Monte Carlo analysis of seismic reflections from Moho and the W reflector. *Journal of Geophysical Research* **102**, 2969–2981.

Musil M., Maurer H.R. and Green A.G. 2003. Discrete tomography and joint inversion for loosely connected or unconnected physical properties – Application to crosshole seismic and georadar data sets. *Geophysical Journal International* **153**, 389–402.

Palacky G.J. 1987. Resistivity characteristics of geologic targets. In: Electromagnetic Methods in Applied Geophysics (ed. M.N. Nabighian), pp. 53–129. SEG.

Revil A., Cathles L.M. and Losh S. 1998. Electrical conductivity in shaly sands with geophysical applications. *Journal of Geophysical Research* **103**, 23925–23936.

Sambridge M., Beghein C., Simons F.J. and Snieder R. 2006. How do we understand and visualize uncertainty?. *The Leading Edge* **25**, 542–546.

Scales J.A. and Tenorio L. 2001. Prior information and uncertainty in inverse problems. *Geophysics* **66**, 389–397.

Snieder R., Xie M.Y., Pica A. and Tarantola A. 1989. Retrieving both the impedance contrast and background velocity – A global strategy for the seismic reflection problem. *Geophysics* **54**, 991–1000.

Spikes K., Mukerji T., Dvorkin J. and Mavko G. 2007. Probabilistic seismic inversion based on rock-physics models. *Geophysics* **72**, R87–R97.

Tarantola A. 2005. *Inverse Problem Theory and Methods for Model Parameter Estimation*. Society for Industrial and Applied Mathematics.

Tenorio L. 2001. Statistical regularization of inverse problems. *SIAM Review* **43**, 347–366.

Tikhonov A.N. and Arsenin V.Y. 1977. *Solution of Ill-posed Problems*. Winston and Sons.

Ulrych T.J., Sacchi M.D. and Woodbury A. 2001. A Bayes tour of inversion – A tutorial. *Geophysics* **66**, 55–69.

Waxman M.H. and Smits L.J.M. 1968. Electrical conductivities in oil-bearing shaly sands. *Society of Petroleum Engineering Journal* **8**, 107–122.

Wood A.W. 1955. *A Textbook of Sound*. The MacMillan Co.

Yilmaz O. 1987. *Seismic Data Processing*. SEG.

APPENDIX A: METROPOLIS-HASTINGS ALGORITHM

The Metropolis-Hastings algorithm (Metropolis *et al.* 1953; Hastings 1970) is a method for generating a sequence of samples from a probability distribution that is difficult to sample directly. The actual implementation of the algorithm is comprises of the following steps.

1 Pick an initial sample $\mathbf{m}_{prev} \in \mathbb{R}^n$ and set $k = 1$, $\mathbf{m}^{(k)} = \mathbf{m}_{prev}$.
2 Set $k \rightarrow k + 1$.
3 Draw a proposal sample $\mathbf{m}_{prop} \in \mathbb{R}^n$ from the proposal distribution $q(\mathbf{m}_{prev}, \mathbf{m}_{prop})$ and calculate the acceptance ratio

$$\alpha(\mathbf{m}_{prev}, \mathbf{m}_{prop}) = \min\left[1, \frac{\pi_{post}(\mathbf{m}_{prop})q(\mathbf{m}_{prop}, \mathbf{m}_{prev})}{\pi_{post}(\mathbf{m}_{prev})q(\mathbf{m}_{prev}, \mathbf{m}_{prop})}\right].$$

(A1)

4 Draw $t \in [0, 1]$ from the uniform probability density.
5 If $\alpha(\mathbf{m}_{prev}, \mathbf{m}_{prop}) \geq t$, set $\mathbf{m}^{(k)} = \mathbf{m}_{prop}$; otherwise, $\mathbf{m}^{(k)} = \mathbf{m}_{prev}$.
6 When k is the desired sample size, stop; otherwise, repeat the procedure starting with step (2).

We choose a Gaussian distribution as a proposal distribution as follows:

$$\mathbf{m}_{prop} \sim N\left(\mathbf{m}_{prev}, \sigma_i^2 \mathbf{I}\right),$$

(A2)

where the variances σ_i^2 describe the probabilistic sampling step of the model parameters during the random simulation. If σ_i^2 is too large, the drawn $\mathbf{m}_{prop}$ is practically never accepted. On the other hand, if σ_i^2 is too small, a proper sampling of the distribution requires a prohibitively large sample set. A good rule of thumb is that roughly 20–30% of all $\mathbf{m}_{prop}$ should be accepted (Kaipio *et al.* 2000).

APPENDIX B: ROCK-PHYSICS MODELS OF THIS STUDY

P-wave velocity V_p is defined as a function of bulk modulus K, shear modulus μ and density ρ, such that

$$V_p = \sqrt{\frac{K + \frac{4}{3}\mu}{\rho}}. \tag{B1}$$

The bulk modulus K is related to porosity ϕ and water saturation S_w. For a fluid saturated medium, the bulk modulus is given by Gassmann's equation (Gassmann 1951; Han and Batzle 2004) as follows:

$$K = K_d + \frac{\left(1 - \frac{K_d}{K_0}\right)^2}{\frac{\phi}{K_f} + \frac{1-\phi}{K_0} - \frac{K_d}{K_0^2}}, \tag{B2}$$

where K_d, K_0 and K_f are the bulk modulus of the dry rock, mineral material and pore fluid, respectively. We model two phases of pore fluid: water and gas. A mixture of two different pore fluids can be regarded as an effective fluid model and the bulk modulus is derived from Wood's equation (Wood 1955; Batzle and Wang 1992) as follows:

$$\frac{1}{K_f} = \frac{S_w}{K_w} + \frac{1 - S_w}{K_g}, \tag{B3}$$

where K_w and K_g are the bulk modulus of the water and gas phases. We also relate the bulk modulus of the dry rock K_d and shear modulus μ with porosity ϕ as follows:

$$K_d = K_0 \left(1 - \frac{\phi}{\phi_c}\right), \tag{B4}$$

$$\mu = \mu_0 \left(1 - \frac{\phi}{\phi_c}\right), \tag{B5}$$

where μ_0 is the shear modulus of the mineral material and ϕ_c is the critical porosity that is the threshold porosity value

between the suspension and the load-bearing domain. Finally, we model the dependence of density ρ on porosity and water saturation as:

$$\rho = \phi S_w \rho_w + (1 - \phi)\rho_0, \tag{B6}$$

where ρ_w and ρ_0 are the density of water phase and mineral material, respectively.

The relationship between the reservoir parameters and electric conductivity is first given by Archie's second law (Archie 1942), which describes electric conductivity in clean sands. In fact, electric conductivity in shaley sands is complicated by the presence of clays and is described by the Waxman-Smits formula (Waxman and Smits 1968):

$$\sigma_e = \phi^m S_w^n \left[\sigma_w + \frac{B Q_v}{S_w}\right], \tag{B7}$$

where m is the cementation exponent, n is the saturation exponent and σ_w is electric conductivity of the pore fluid. The parameter B is an equivalent counterion mobility and Q_v is the excess of surface charge per unit pore volume. Parameter B is given empirically at 25°C by

$$B = B_0 \left[1 - 0.6 \exp\left(-\frac{\sigma_w}{0.013}\right)\right], \tag{B8}$$

where σ_w is in S/m and the maximum counterion mobility B_0 is given by 4.78×10^{-8} m^2/V/s (Revil, Cathles and Losh 1998). Parameter Q is related to the mineral density ρ_0 (in kg/m^3) and the cation exchange capacity (CEC) by

$$Q_v = \rho_0 \frac{1 - \phi}{\phi} \text{CEC}. \tag{B9}$$

The cation exchange capacity is only significant for clay minerals and the variation of cation exchange capacity for different clay minerals is dramatic.

The modelled values of each rock-physics parameters introduced above are summarized in Table 1.